Predicting microstructures in polymer blends under two-step quench in two-dimensional space

Y. C. Li,[1,2] R. P. Shi,[1,3] C. P. Wang,[1] X. J. Liu,[1,*] and Y. Wang[3,†]

[1]*Department of Materials Science and Engineering, College of Materials, and Research Center of Materials Design and Applications, Xiamen University, Xiamen 361005, People's Republic of China*

[2]*Department of Mechanical Engineering, Xiamen University of Technology, Xiamen, 361024, People's Republic of China*

[3]*Department of Materials Science and Engineering, The Ohio State University, 2041 College Road, Columbus, Ohio 43210, USA*

(Received 21 November 2010; published 15 April 2011)

The formation of nanostructures during two-step quench in binary polymer systems having various types of liquid miscibility gaps are investigated systematically via computer simulations using the phase field method. Coupled liquid spinodal decomposition and fluid flow processes are considered by solving simultaneously the Cahn-Hilliard and Navier-Stokes equations. Various interesting phenomena and morphological patterns are predicted. It is found that the primary microstructures developed at the first quench and isothermal holding temperature greatly affect the secondary microstructures developed during the second quench and isothermal holding. Depending on the morphology and scale of the primary microstructure, either multicore and multishell or unicore and unishell structures are predicted. The breakup of annuluses in a core-shell structure in two dimensions is analyzed. The effects of viscosity on the formation of core-shell structure and on the growth and coarsening behaviors of bimodal droplets produced by the two-step quench in systems are also investigated.

DOI: 10.1103/PhysRevE.83.041502 PACS number(s): 64.70.Ja, 64.75.Va, 64.60.Bd, 64.70.km

I. INTRODUCTION

When two polymers mutually dissolve, various types of miscibility gaps exist, which are different from those observed in small molecule systems and thus offer opportunities for morphological pattern design through phase separation in polymer blends via different processes [1,2], such as thermal-induced phase separation (TIPS), nonsolvent-induced phase separation (NIPS), and polymerization-induced phase separation (PIPS) methods [3–5]. Recently, interesting heat treatment procedures such as two-step quench have gained much interest from researchers [6–11]. A two-step quench consists of a first shallow quench into the miscibility gap from a single-phase region followed by a second deep quench into the miscibility gap [6], as schematically shown in Fig. 1. The two-step quench has produced unique nanostructures [7] that, to the best of our knowledge, have not been observed in the usual single-step quench experiments. In addition, the hierarchic microstructures induced by a two-step quench were found to have complex coarsening characteristics [6–11]. Thus, a detailed understanding of phase separation processes during a two-step quench leading to various two-phase mixtures is of both fundamental interest and practical importance.

Therefore, extensive numerical simulations have been carried out [2], [12–16] to study pattern formation under different two-step quench conditions. Podariu *et al*. [2] studied a two-step quench process in an asymmetric binary mixture having an upper critical solution temperature (UCST) and showed that the average size of the secondary domains increased with the increasing depth of the second quench and the increasing initial quench temperature at a fixed depth of the two-step quench. Clarke *et al*. [12,13] investigated phase separation in a symmetric binary polymer system using the Flory-Huggins thermodynamic model and the Cahn-Hilliard kinetic equation. They mainly considered the early stage of a two-step quench and studied the effect of quench depth. They also quantified the kinetics of microstructural evolution using the time-dependent structure factor. Chan *et al*. [14] studied the two-step thermal-induced phase separation phenomenon in symmetric polymer blends via spinodal decomposition in one dimension. They indicated that a dimensionless diffusion coefficient may be used as a parameter to control the formation and evolution of the phase-separated regions. Huang *et al*. [15] used a so-called cell dynamical system (CDS) simulation method to investigate phase separation of binary polymer blends contacted with an external surface under two-step quench conditions. They observed that a deeper second quench into the miscibility gap favored the formation of lamellar structures.

In all, former works mainly focus on the effects of the quench depth during the two-step quench, either the first or the second one. Besides, in all of the simulation studies [2], [12–16], the effect of hydrodynamic flow was ignored for simplicity. However, polymer belongs to the categories of "soft matter" or "complex fluids" [17,18], and hydrodynamic flow has been shown to play an important role during phase separation [19–21]. On the other hand, the kinetic process of phase separation is also important for pattern formation and pattern selection in polymer materials science. Therefore, it is necessary to know the mechanisms and the formation kinetics of unique morphologies during the two-step quench.

While there has been an enormous movement to study experimentally [3,8,22–24] and theoretically [2,12,13,25–28] the phase behavior of polymer blends in three-dimensional (3D) systems, little work has focused on the understanding of phase separation in a confined two-dimensional (2D) space. However, the construction of nanoscopic devices [29–31] has attracted great attention, and the use of polymer thin films in technology is increasingly widespread [32], which demands a better understanding of the phase behavior of fluids confined in pores or slits. Thus, an understanding of the microstructure evolution confined in 2D space is important for developing materials.

*lxj@xmu.edu.cn
†wang.363@osu.edu

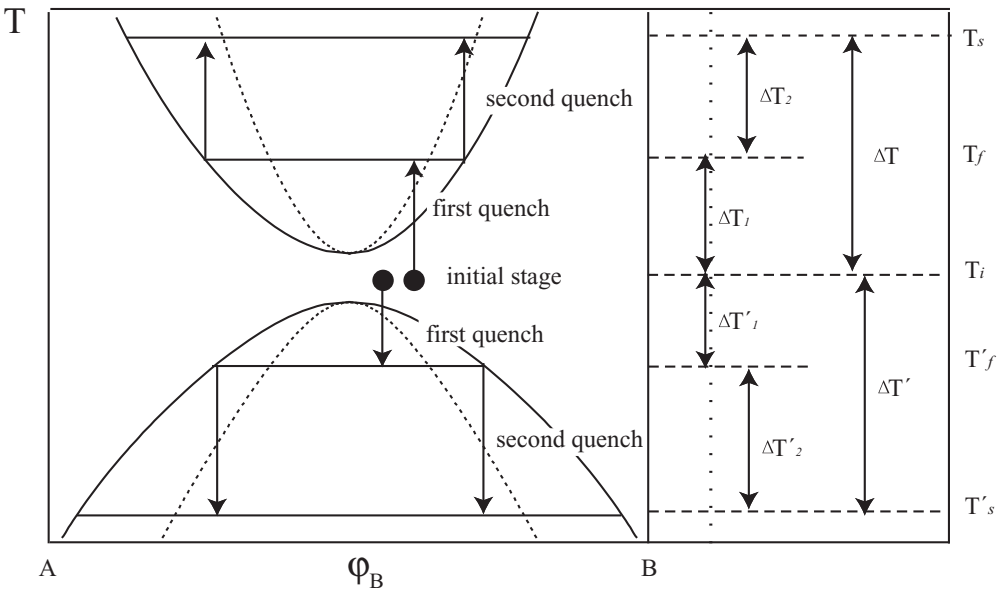

FIG. 1. Schematic diagram for two-step heat treatment. A system is first quenched from T_i to T_f (LCST) or T_f' (UCST) and isothermally held for a given period of time. Then it is quenched again to T_s (LCST) or T_s' (UCST) and isothermally held for another given period of time.

In this paper we systematically investigate pattern formation and pattern stability in binary polymer systems having various types of miscibility gaps under two-step quench conditions in 2D space via computer simulations using the phase field method. The main objective is to develop a fundamental understanding of how alloy composition, quench history, and material parameters affect the kinetic pathway of the two-step phase separation process. In particular, we show that a rich variety of unique nanostructures could be produced by simple two-step heat treatments. The model simultaneously considered coupled phase separation and hydrodynamic flow. The paper is organized as follows. The thermodynamic model and kinetic equations are described in the proceeding section. Major simulation results are presented in Sec. III, including various morphological patterns such as multicore and multishell and unicore and unishell structures. The breakup of interconnected microstructures in a 2D system, the formation of core-shell structures, and the growth and coarsening characteristics of bimodal two-step quench microstructures in systems having different viscosities are analyzed in Sec. IV. Major findings are summarized in Sec. V.

II. MODEL AND SIMULATIONS

A. Thermodynamic model

The free-energy density is described by the Flory-Huggins model [33],

$$f_{\text{vol}}(\varphi) = \frac{1}{V_m} f(\varphi), \tag{1}$$

with

$$f(\varphi) = RT\left[\frac{1}{N_1}(1-\varphi)\ln(1-\varphi) + \frac{1}{N_2}\varphi\ln\varphi\right] + \chi\varphi(1-\varphi), \tag{2}$$

where N_i and φ are the degree of polymerization of component i and volume fraction of polymer B (equivalent to mole fraction if polymers A and B have the same molar volume), respectively. V_m is the molar volume of the mixture and χ is the interaction parameter determining the enthalpy contribution toward mixing. χ is usually expressed as a function of temperature T in the following empirical form [34]:

$$\chi = A + BT + DT\ln T. \tag{3}$$

A, B, and D are parameters which need to be evaluated. On the basis of Eqs. (1)–(3), a binary phase diagram can be calculated.

B. Kinetic model

According to Cahn-Hilliard theory [35], the diffusion equation describing phase separation kinetics can be written as

$$\frac{\partial\varphi}{\partial t} = M\nabla^2\left[\frac{\partial\,[f_{\text{vol}}(\varphi)]}{\partial\varphi} - 2\kappa(\varphi)\nabla^2\varphi\right] + \zeta(r,t), \tag{4}$$

where M is the chemical mobility (assumed to be composition independent), $\zeta(r,t)$ is the noise term, $\kappa(\varphi)$ is the gradient energy coefficient that can be derived by using a mean-field treatment of correlations in polymer mixtures known as the random phase approximation (RPA) [36],

$$\kappa(\varphi) = \frac{\chi r_0^2}{6} + \frac{a^2 RT}{36\varphi(1-\varphi)}, \tag{5}$$

where r_0 is the range of interactions and a is the statistical segment length. The first term in Eq. (5) is derived from a lattice gas model, and the second term originates from the entropic penalty arising from the restriction of chain configurations in

steep concentration gradients. The mobility can be expressed as

$$M = \frac{D(T)(1-\varphi_{\text{initial}})\varphi_{\text{initial}} V_m}{RT}, \tag{6}$$

fwhere $D(T)$ is the chemical diffusivity as a function of temperature T and φ_{initial} is the volume fraction of polymer B.

When fluid flow is considered, the kinetic equation with a convection term $(\vec{u}\cdot\vec{\nabla})\varphi$ reads as follows [37,38]:

$$\frac{D\varphi}{Dt} = \frac{\partial\varphi}{\partial t} + \vec{u}\cdot\vec{\nabla}\varphi = M\nabla^2\left[\frac{\partial\left[f_{\text{vol}}(\varphi)\right]}{\partial\varphi} - 2\kappa(\varphi)\nabla^2\varphi\right], \tag{7}$$

where $\frac{D}{Dt}$ indicates the material derivative and is defined as $\frac{D\varphi}{Dt} = \frac{\partial\varphi}{\partial t} + (\vec{u}\cdot\vec{\nabla})\varphi$, and $\vec{u}$ is the fluid velocity vector.

The Navier-Stokes equation coupled with the Cahn-Hilliard equation is used to characterize the contributions from fluid flow during phase separation. Here we consider an incompressible viscous liquid having a constant mass density. Then the continuity and momentum equations read as follows:

$$\vec{\nabla}\cdot\vec{u} = 0, \tag{8}$$

$$\rho_0\frac{D\vec{u}}{Dt} = \rho_0\left(\frac{\partial\vec{u}}{\partial t} + \vec{u}\cdot\vec{\nabla}\vec{u}\right) = -\vec{\nabla}S - \varphi\vec{\nabla}\mu_\varphi + \eta\nabla^2\vec{u}, \tag{9}$$

where ρ_0 is the mass density, η is the viscosity coefficient, the term $-\varphi\vec{\nabla}\mu_\varphi$ is the continuum surface tension force [39], and S includes the pressure and other effects which enforce the incompressibility.

Following Jacqmin [39], the first two terms on the right-hand side of Eq. (9) can be expressed as

$$-\vec{\nabla}S - \varphi\vec{\nabla}\mu_\varphi = -\vec{\nabla}P + \vec{\nabla}\cdot\vec{\tau}, \tag{10}$$

where $\vec{\nabla}P$ is the pressure gradient, and $\vec{\nabla}\cdot\vec{\tau}$ is a stress forcing term. Therefore, the momentum equation in 2D can be given as follows:

$$\rho\left(\frac{\partial u}{\partial t} + u\frac{\partial u}{\partial x} + v\frac{\partial u}{\partial y}\right) = -\frac{\partial p}{\partial x} + 2\kappa(\varphi)\left[-\frac{\partial^2\varphi}{\partial x^2}\left(\frac{\partial\varphi}{\partial x}\right) - \frac{\partial^2\varphi}{\partial y^2}\left(\frac{\partial\varphi}{\partial x}\right)\right] + \eta\left[\frac{\partial^2 u}{\partial x^2} + \frac{\partial^2 u}{\partial y^2}\right] \tag{11}$$

along the x direction and

$$\rho\left(\frac{\partial v}{\partial t} + u\frac{\partial v}{\partial x} + v\frac{\partial v}{\partial y}\right) = -\frac{\partial p}{\partial y} + 2\kappa(\varphi)\left[-\frac{\partial^2\varphi}{\partial x^2}\left(\frac{\partial\varphi}{\partial y}\right) - \frac{\partial^2\varphi}{\partial y^2}\left(\frac{\partial\varphi}{\partial y}\right)\right] + \eta\left[\frac{\partial^2 v}{\partial x^2} + \frac{\partial^2 v}{\partial y^2}\right] \tag{12}$$

along the y direction. In Eqs. (11) and (12), u and v are the x and y components of $\vec{u}$.

C. Governing equations in dimensionless forms

Equations (7), (11), and (12) are reduced into dimensionless forms using the following relationships:

$$\tau = \frac{l^2}{D'_\infty}, \tag{13}$$

$$t = \tau\cdot t^* = \frac{l^2}{D'_\infty}t^*, \tag{14}$$

$$x = l\cdot x^*, \tag{15}$$

$$u = \frac{D'_\infty}{l}u^*, \tag{16}$$

$$v = \frac{D'_\infty}{l}v^*, \tag{17}$$

$$p = Cp^*, \tag{18}$$

where τ is defined as the characteristic diffusion time scale of polymers, and D'_∞ is the characteristic value of system diffusivity. C is the dimensionless parameter of pressure, and the scaling length l can be determined according to the interface thickness.

Using Eqs. (13)–(19), Eqs. (7), (11), and (12) become

$$\frac{\partial\varphi(t^*)}{\partial t^*} + \vec{u}^*\frac{\partial\varphi}{\partial x^*} + v^*\frac{\partial\varphi}{\partial y*} = \frac{D(T)}{D'_\infty}\varphi(1-\varphi)\nabla^{*2}\left[\frac{\partial\left[f(\varphi)/RT\right]}{\partial\varphi} - 2\kappa(\varphi)\frac{V_m}{RT}\frac{1}{l^2}\nabla^{*2}\varphi\right] + \varsigma'(r,t^*), \tag{19}$$

$$\rho_0\left(\frac{\partial u^*}{\partial t^*} + u^*\frac{\partial u^*}{\partial x^*} + v^*\frac{\partial u^*}{\partial y^*}\right) = -C\frac{l^2}{D'^2_\infty}\frac{\partial p^*}{\partial x^*} + 2\kappa(\varphi)\frac{1}{D'^2_\infty}\left[-\frac{\partial^2\varphi}{\partial x^{*2}}\left(\frac{\partial\varphi}{\partial x^*}\right) - \frac{\partial^2\varphi}{\partial y^{*2}}\left(\frac{\partial\varphi}{\partial x^*}\right)\right] + \eta\frac{1}{D'_\infty}\left[\frac{\partial^2 u^*}{\partial x^{*2}} + \frac{\partial^2 u^*}{\partial y^{*2}}\right], \tag{20}$$

$$\rho_0\left(\frac{\partial v^*}{\partial t^*} + u^*\frac{\partial v^*}{\partial x^*} + v^*\frac{\partial v^*}{\partial y^*}\right) = -C\frac{l^2}{D'^2_\infty}\frac{\partial p^*}{\partial y^*} + 2\kappa(\varphi)\frac{1}{D'^2_\infty}\left[-\frac{\partial^2\varphi}{\partial x^{*2}}\left(\frac{\partial\varphi}{\partial y^*}\right) - \frac{\partial^2\varphi}{\partial y^{*2}}\left(\frac{\partial\varphi}{\partial y^*}\right)\right] + \eta\frac{1}{D'_\infty}\left[\frac{\partial^2 v^*}{\partial x^{*2}} + \frac{\partial^2 v^*}{\partial y^{*2}}\right]. \tag{21}$$

III. SIMULATION RESULTS

A. Phase diagram calculation

Various types of binary phase diagrams of polymer systems are calculated according to the Flory-Huggins model by optimizing parameter χ, as presented in Fig. 2, where the dark solid curve represents the binodal (equilibrium curve) and the light dashed curve represents the spinodal one. As we can see, most polymer blends exhibit a lower critical solution

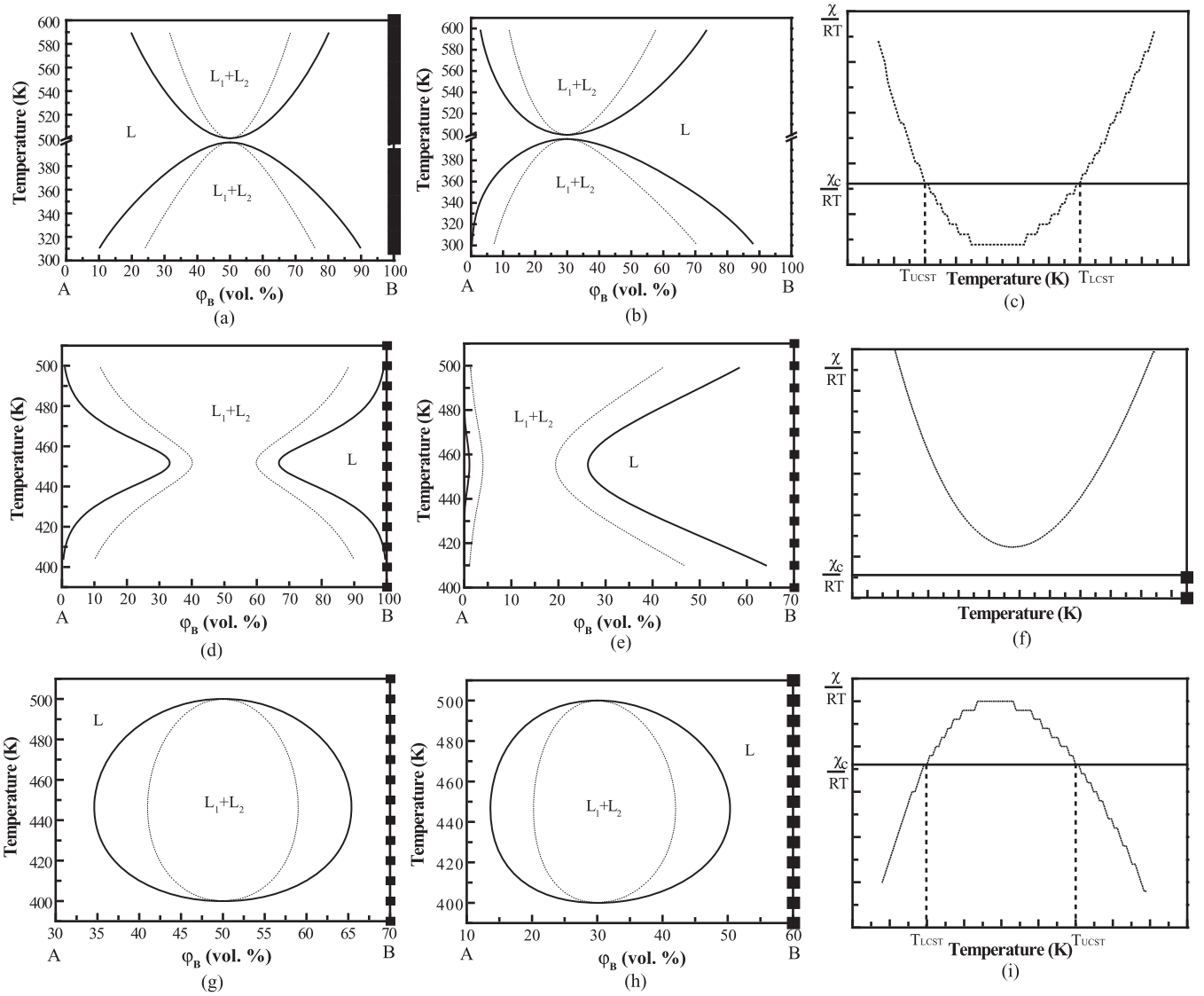

FIG. 2. Different types of phase diagrams for various polymer blends and temperature dependences of the interaction parameter. A blend with a LCST above a UCST: (a) symmetrical and (b) asymmetrical. A blend with a tendency toward greater solubility at intermediate temperatures (hourglass-type phase diagram): (d) symmetrical and (e) asymmetrical. A blend with a UCST above a LCST (closed-phase diagram): (g) symmetrical and (h) asymmetrical. In these figures, the solid lines represent binodal, and the dashed lines represent spinodal. The temperature dependence of the interaction parameter and its effect on the liquid-liquid equilibrium for the three systems are presented in (c), (f), and (i), respectively.

temperature (LCST), a UCST, a closed loop, or an hourglass phase diagram.

According to the Flory-Huggins model, the critical condition ($\frac{\partial^3 f_{\mathrm{vol}}(\varphi)}{\partial \varphi_2^3} = 0$) yields

$$RT\left(\frac{1}{N_1\varphi_1^2} - \frac{1}{N_2\varphi_2^2}\right) - \frac{6\partial\chi}{\partial\varphi_2} + 3(1-2\varphi_2)\frac{\partial^2\chi}{\partial\varphi_2^2} + \varphi_1\varphi_2\frac{\partial^3\chi}{\partial\varphi_2^3} = 0. \tag{22}$$

If χ does not depend on concentration, Eq. (22) leads to the following condition for the critical point:

$$\varphi_{2c} = \frac{\sqrt{N_1}}{\sqrt{N_1}+\sqrt{N_2}}. \tag{23}$$

And then the critical interaction parameter can be derived:

$$\frac{\chi_c}{RT} = 1/2\left(N_1^{-1/2} + N_2^{-1/2}\right)^2. \tag{24}$$

When both N_1 and N_2 are large (polymer mixtures), χ_c is very small. If $N_1 = N_2$, $\varphi_{2c} = 0.5$, the miscibility gap is symmetrical; otherwise the miscibility gap is asymmetrical. The temperature dependence of the interaction parameter and its effect on liquid-liquid equilibrium are sketched in Fig. 2. As presented in Figs. 2(c), 2(f), and 2(i), if $\chi < \chi_c$, the mixture will be a single liquid phase in all composition. In Fig. 2(c), χ is equal to χ_c at T_{UCST} and T_{LCST}. At temperatures $T < T_{\mathrm{UCST}}$ and $T > T_{\mathrm{LCST}}$, χ is larger than χ_c, and then there exists the miscibility gap of liquid phase, as in Fig. 2(b). However, in Fig. 2(i), the miscibility gap exists at a temperature range

TABLE I. Summary of the Flory-Huggins model parameters used in calculating the phase diagram shown in Fig. 2.

Parameter	Value					
	Symmetric system with LCST and UCST	Asymmetric system with LCST and UCST	Symmetric system of "hourglass type"	Asymmetric system of "hourglass type"	Symmetric system of "circle type"	Asymmetric system of "circle type"
T_{UCST}	400	400	—	—	500	500
T_{LCST}	500	500	—	—	400	400
N_1	100	90	100	90	100	90
N_2	100	490	100	490	100	490
φ_{crit}	0.5	0.3	—	—	0.5	0.3
χ	$400 - 6.2038T$ $+0.8963T \ln T$	$400 - 6.2758T$ $+0.8963T \ln T$	$0.05T^2 - 45T$ $+10203$	$0.5T^2 - 450T$ $+103682$	$-400 + 6.5363T$ $-0.8963T \ln T$	$-400 + 6.4643T$ $-0.8963T \ln T$

from T_{LCST} to T_{UCST}. In Fig. 2(f), χ is always larger than χ_c, therefore, there may be liquid-liquid phase separation at all temperatures. The model parameters used in the calculation are listed in Table I.

B. Microstructural evolution during double quench

Even though the thermodynamic model used in the current study is for polymer systems, the obtained simulation results should be general for any systems having a miscibility gap. All phase field simulations are carried out in 2D and the system size is $256\Delta x_1 \times 256\Delta x_2$ with $\Delta x_1 = \Delta x_2 = 9$ nm. Periodical boundary conditions are applied along both dimensions.

According to Fig. 1, if an alloy is quenched from T_f to T_s (in the LCST of Fig. 1), then the secondary spinodal decomposition only proceeds in one of the domains [B-rich phase, which the volume fraction of polymer B is larger than 0.5, in red (light gray)] produced by the first quench (primary spinodal decomposition) because the other primary domain [A-rich phase, represented as the color blue (dark gray)] has an initial composition between the miscibility and the spinodal curves at the second-quench temperature, which defines the metastable region [40]. However, if the second quench is from T_f' to T_s' (in the UCST of Fig. 1), both primary domains become unstable (in the spinodal region) during the second quench. Simulation results obtained from each of these two cases will be presented in the following section.

(1) Both types of primary domains undergo secondary spinodal decomposition. The simulation of microstructure evolution during a two-step quench from the region outside of the miscibility gap to 515 K until the system reaches the equilibrium composition and then to 590 K in the system with LCST [Fig. 3(a)] was carried out. During the simulation, the viscosity of the system is assumed to be 1 Pa s. Typical microstructure evolutions during the second quench from 515 to 590 K having an initial volume fraction of polymer B of 0.25 are presented in Fig. 4. The micrograph at reduced time $\tau = 0$ is the final two-phase microstructure obtained during isothermal holding (aging) at the first quenching temperature (515 K), which is also the initial microstructure for the second quench and aging at 590 K. At an early stage of the second aging, spinodal decomposition independently proceeds in both domains of the primary phases formed during the first aging temperature. The morphology and scale of the preexisting structure have a strong effect on the spinodal decomposition process and leads to unique microstructures. For example, interesting multicore and multishell and single-core and multishell structures are readily found in Figs. 4(b) and 4(c), which at a later stage coarsen to single-domain particles having equilibrium compositions corresponding to the new aging temperature. An interesting observation during the coarsening process is the breakup of the shells into discrete particles, which will be further analyzed later in Sec. IV A. Droplet drifting, collision, and coagulation caused by hydrodynamic effects take place among the small droplets formed during the second quench, which make the coarsening kinetics significantly deviate from the Lifshitz-Slyozov-Wagner (LSW) theory [41] (see Sec. IV C for details).

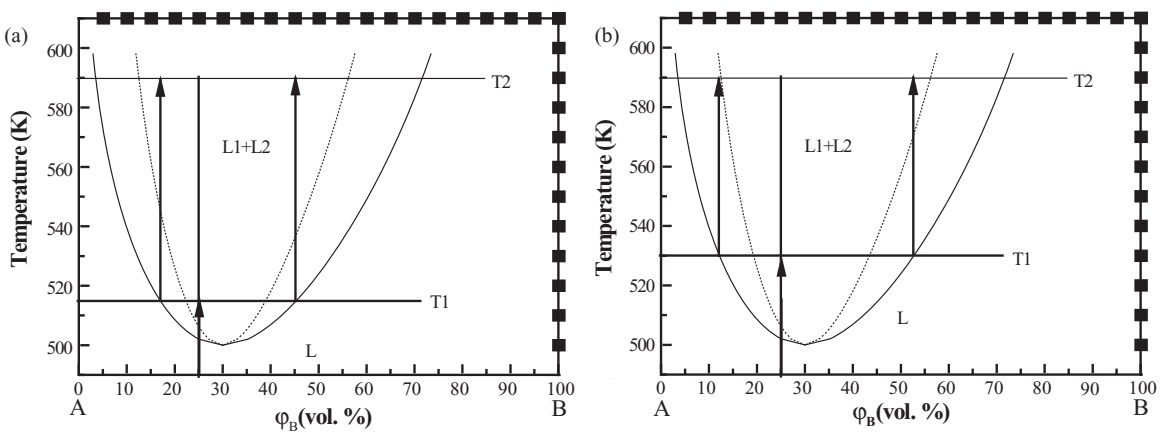

FIG. 3. Schematic phase diagram of two-step quench process of the simulation. (a) From 515 to 590 K; (b) from 530 to 590 K.

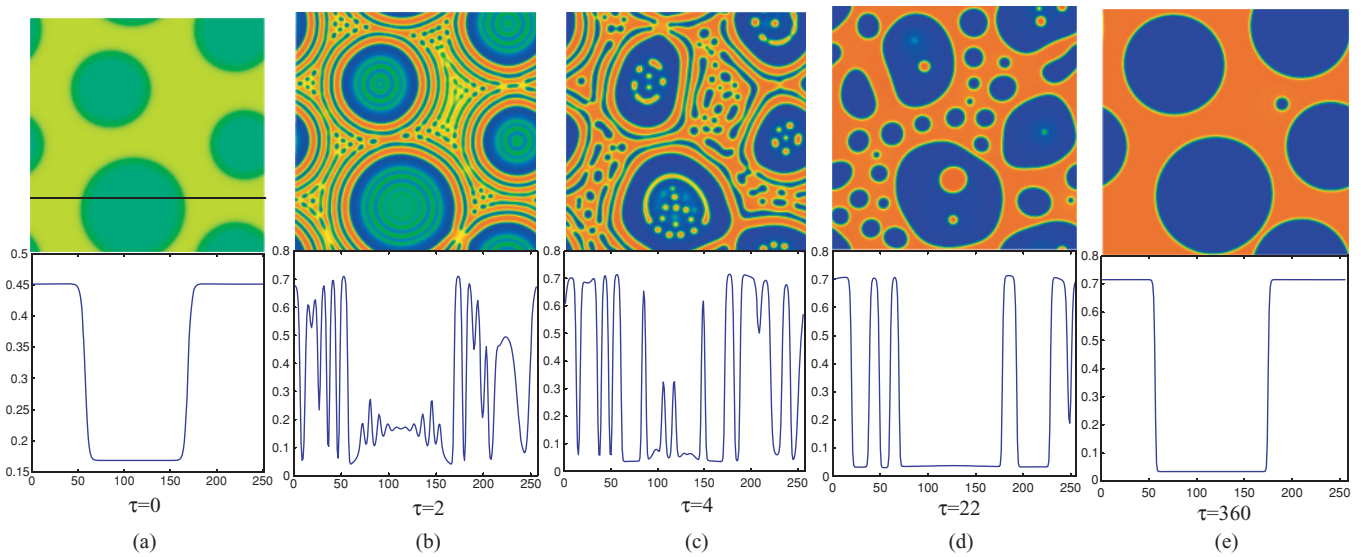

FIG. 4. (Color online) Phase field simulation of pattern evolution and the corresponding concentration profile along the line indicated in (a) caused by a double quench from 515 to 590 K at different quench times.

(2) One type of primary domain undergoes secondary spinodal decomposition. Figure 5 shows a typical microstructure evolution when the secondary spinodal decomposition only proceeds in the matrix phase (*A*-rich phase) that resulted from the primary spinodal decomposition. The procedure of two-step quench treatment is presented in Fig. 3(b). When the two-phase microstructure ($\tau = 0$) obtained from the first quench at 530 K is quenched again to a temperature deeper inside the miscibility gap (590 K), the *B*-rich phase becomes unstable while the *A*-rich phase becomes metastable. Spinodal decomposition takes place only in the *B*-rich phase, and nucleation proceeds in the *A*-rich phase. However, in our simulation, we mainly considered the spinodal decomposition. No thermal fluctuation is induced during the second quench. Thus, no nucleation takes place in the *A*-rich phase. As shown in Fig. 5, at the very early stage of the second quench, clear "halo"-type annuluses form around the primary domains. Then the annuluses break up into small domains, leading to a typical bimodal microstructure. At a later stage, the small secondary droplets in the *B*-rich phase disappear due to coarsening and collision. A simulation of a two-step quench from 455 to 480 K in an asymmetric "hourglass-type" system [Fig. 2(e)] produces similar microstructures.

IV. DISCUSSIONS

A. Formation and breakup of annuluses

As presented in Figs. 4 and 5, annular shell structures immediately form after the second deep quench. Halo-type structures are observed, which agrees well with the simulations of Huang *et al*. [15] on the effect of fillers and the simulations of Shen *et al*. [42] on effect of dislocations on spinodal decomposition. In these cases, the preexisting concentration

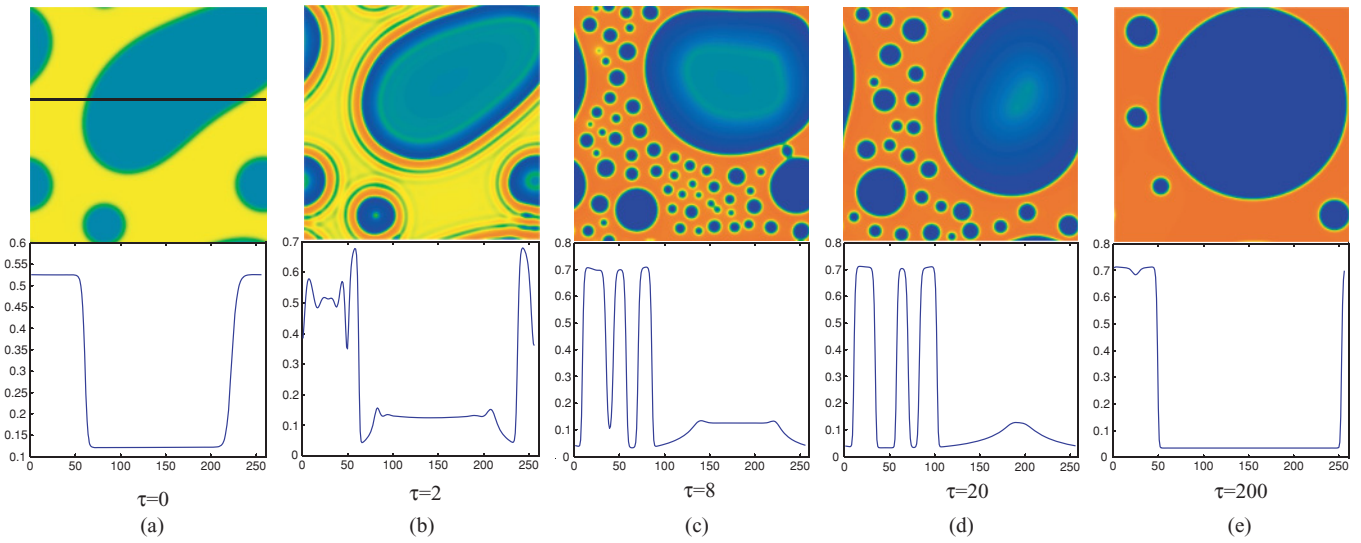

FIG. 5. (Color online) Phase field simulation of pattern evolution and the corresponding concentration profile along the line indicated in (a) caused by a double quench from 530 to 590 K at different quench times.

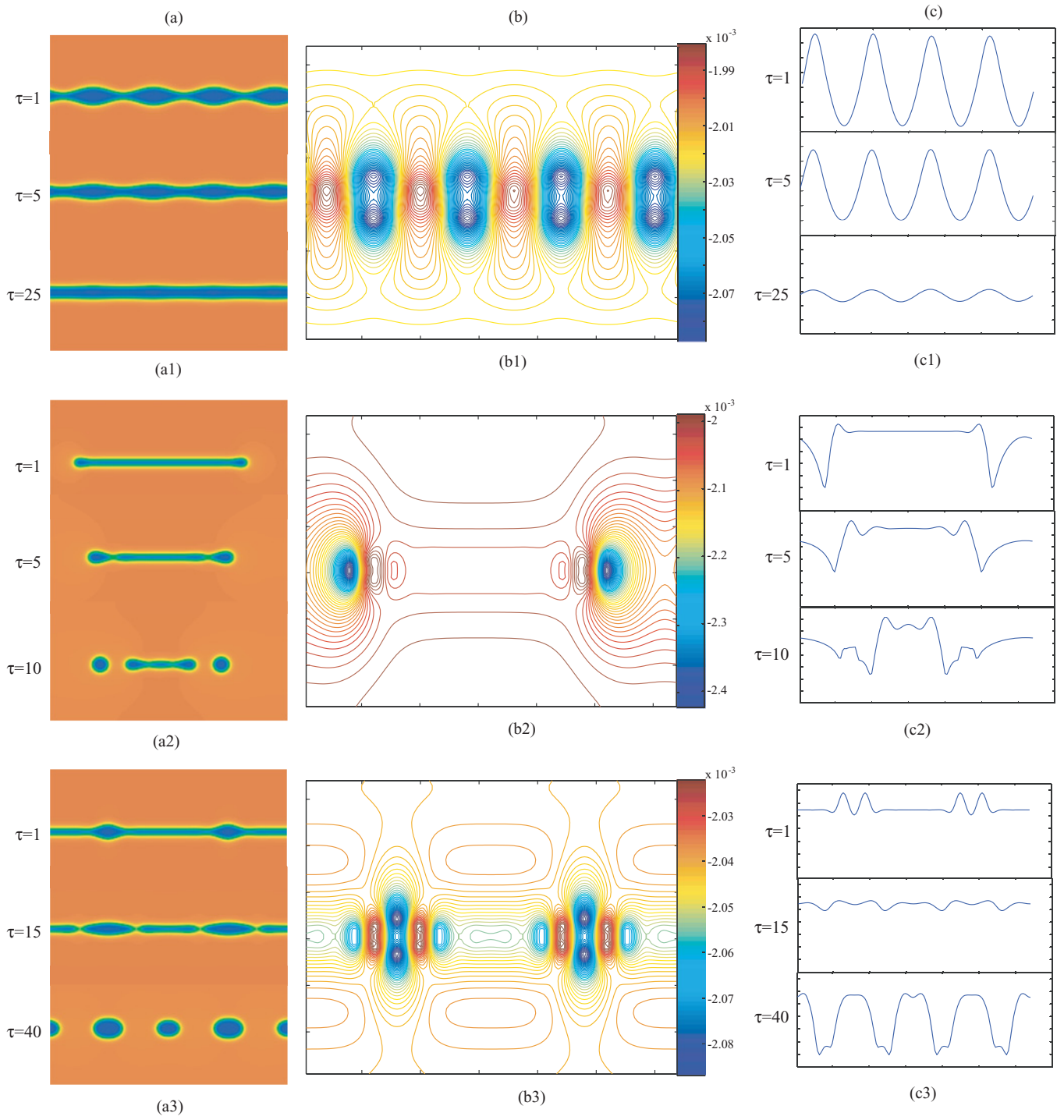

FIG. 6. (Color online) Effect of initial condition on the stability of strips. (a1) Sinusoidal-shaped perturbation of an infinite strip; (a2): rod-shaped perturbation of a finite strip; (a3) dumbbell-shaped perturbation of an infinite strip. The corresponding chemical potential contours at the initial stage are shown in (b1)–(b3) and the time evolution of the chemical potential along the central line across the thread are shown in (c1)–(c3).

nonuniformity enhances the spinodal decomposition process and leads to the observed microstructures. However, if the second quench is not deep enough, the composition rings may break up into droplets before the appearance of a clear shell structure.

It is observed that the annular shell structures break up after several time steps. The breakup of the annuluses is driven by interfacial energy reduction, similar to the Rayleigh instability [43,44], which is widely known in 3D systems. However, it has been reported by Miguel that Rayleigh instability is absent in 2D [45]. Almgren suggested that the formation of singularity drove the breakup of the interconnect structure in 2D systems and described a 2D Hele-Shaw effect [46,47]. In our work, further simulation studies (Fig. 6) show that

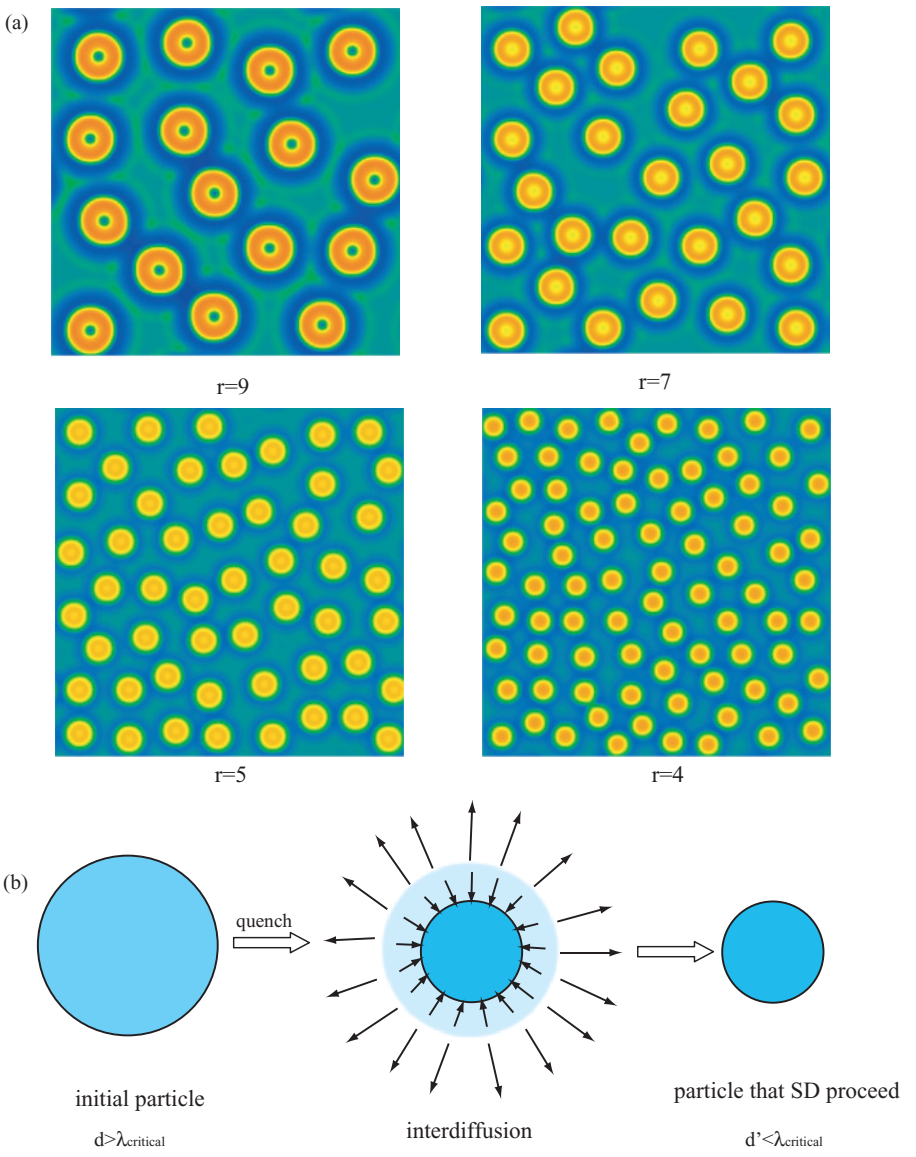

FIG. 7. (Color online) (a) Patterns formed at second-step quench starting with different initial particle sizes from the first quench. (b) Schematics of the composition change of primary particles (formed during the first quench) during the second quench.

the annulus breakup observed in the simulations is due to changes in boundary and initial conditions. As shown in Fig. 6(a1), if the thread is infinite, then it is stable against the introduced sinusoidal perturbation. The chemical potential ($\mu_B - \mu_A = \frac{\delta F}{\delta \varphi}$) field corresponding to Fig. 6(a1) is presented in Fig. 6(b1). The diffusion should occur down along the chemical potential gradient, which indicates that the diffusion process will eliminate the initial perturbation. Figure 6(c1) shows the time evolution of the chemical potential along the central line across the thread. However, the thread will break up into droplets if it is finite, as shown in Fig. 6(a2), or if a different type of perturbation is imposed [Fig. 6(a3)]. In these cases, the curvature is zero at the midpoint of the thin neck and becomes negative at the end of the neck. Therefore, the chemical potential gradient [Figs. 6(b2) and 6(b3)] associated with these nonuniform curvature distributions along the surface of the thread will drive the flow from the middle of the neck toward the end of the neck, causing the breakup.

B. Formation of "core-shell" structures

As shown in Fig. 4, various "core-shell" structures may form during the second quench. Several factors that may affect the formation of the core-shell structures are investigated. It is found that the formation of cores in the core-shell structures strongly depends on the size of the primary domains. Figure 7(a) shows the core-shell microstructures obtained during the second quench of primary microstructures with different domain sizes. It is clearly shown that no core forms during the second quench if the initial particles are too small, for example, when the radius of the particles r equals 36 nm ($r = 4$ grids). According to Cahn's theory on spinodal decomposition [35], the critical wavelength of the microstructure in the second quench is ~45 nm, which is smaller than the diameter of the particle. The reason why no core-shell structure forms is due to the interdiffusion. The primary particles are in contact with the matrix phase and both of them have nonequilibrium compositions at the second quench temperature. Interdiffusion between the particles and

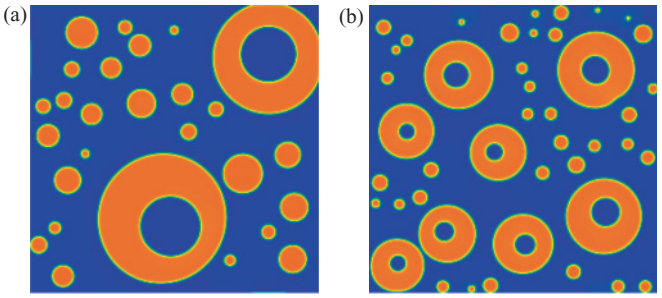

FIG. 8. (Color online) Phase field simulation of pattern formation during a double quench in systems of different viscosities: (a) Viscosity = 0.1 Pa s and (b) viscosity = 1 Pa s.

the matrix will reduce the primary particle size, which may be smaller than the critical wavelength of spinodal decomposition, as schematically shown in Fig. 7(b). Besides, the simulations show that as the size of the particles increases, the time needed to form single core-shell structures increases.

The viscosity of the system also plays an important role in the formation of the core-shell structures. Phase separation patterns considering different viscosity coefficients are presented in Fig. 8. In high viscosity systems, small secondary particles disappear via an evaporation-condensation coarsening mechanism before they coalesce to form the core during the second quench. The volume ratio of core to shell decreases as the viscosity increases. As shown in Fig. 8, the ratio of the core (A-rich phase) to the shell (B-rich phase) is ~33% in Fig. 8(a) where the viscosity is 0.1 Pa s, while in Fig. 8(a) where the viscosity is 1 Pa s, the ratio is ~18%.

C. Growth and coarsening of bimodal droplets

Simulations of a two-step quench from outside of the miscibility gap to 515 K and then to 570 K in a symmetrical system [Fig. 3(a)] considering with various viscosities is carried out to investigate the coarsening behavior of bimodal droplets. A typical particle size evolution with time in a case with fluid flow is presented in Fig. 9(a). Some phase separation patterns are shown in the inset in Fig. 9(a). The growth law of the particle size can be expressed by an equation in the form $r^n - r_0^n = k(t - t_0) + b$, where r_0 is the initial mean particle size at the beginning of the coarsening process [41]. In this simulation, the particle size at total time steps (=2), when the system reached the equilibrium volume fraction, is chosen as r_0. The value of n is determined by R^2 (square of regression coefficient) of the fitting line. In this system, when n equals 2.5, R^2 reaches the maximal value. Figure 9(b) shows the characteristic particle size of the droplets $r^{2.5} - r_0^{2.5}$ after a second quench to 570 K, with the equation of fitting line and R^2.

Further investigations of the growth mechanism of small droplets caused by the second quench in systems having various viscosities are carried out. According to the equation $r^n - r_0^n = k(t - t_0) + b$, if r_0 is small compared with r for the time interval of interest, then n can be obtained from the reciprocal of the slope of ln r vs ln t plot. In this paper, data after r^3 becomes greater than $6r_0^3$ are used in the plots (Fig. 10) [48]. The equations and R^2 of the fitting

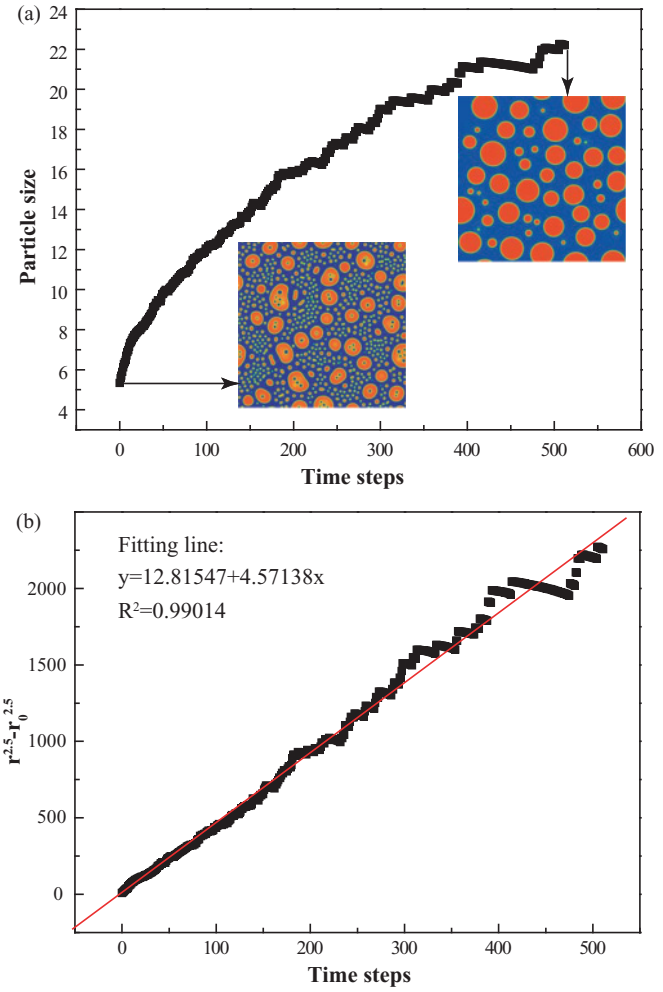

FIG. 9. (Color online) Coarsening kinetics of a bimodal microstructure. The particle size in an average over both populations of large and small particles.

lines are presented in Table II. According to the calculated results, we can find that the line rotates toward higher slopes

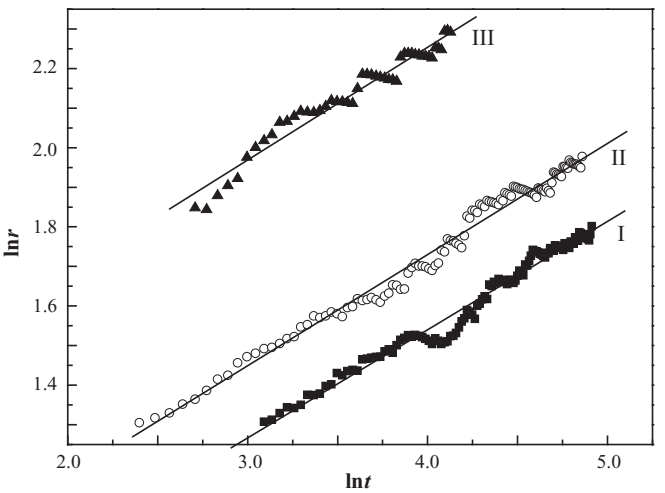

FIG. 10. Double-logarithmic plot of characteristic particle size r of the small droplets vs time t in systems of different viscosities: I (■) viscosity coefficient $\eta = \infty$; II (○) $\eta = 1$; III (▲) $\eta = 0.1$.

TABLE II. Equations and R^2 of the fitting lines with various viscosities shown in Fig. 10.

Viscosity	Equation of fitting line	R square
$\eta \to \infty$	$\ln r = 0.27361 \ln t + 0.44579$	0.97617
$\eta = 1$ Pa s	$\ln r = 0.28086 \ln t + 0.6065$	0.98373
$\eta = 0.1$ Pa s	$\ln r = 0.28479 \ln t + 1.11466$	0.95543

(counterclockwise) when the viscosity is reduced. This implies that the hydrodynamic effect will accelerate the growth of the small droplets.

V. SUMMARY

Unique nanostructures created by a two-step quench in polymer blends in 2D systems are investigated systematically via computer simulations. When both types of the primary domains become unstable during the second quench, multicore and multishell structures are observed at the early stages of the second quench. The shells break up into discrete particles at later stages. If the primary domains are relatively small or only one type of the primary domains becomes unstable during the second quench, single-core and single-shell structures can be formed. During the pattern evolution, bimodal microstructures are observed.

The formation and stability of these microstructures are analyzed. The breakup of the shells in 2D is found to be driven by a chemical potential gradient. The formation of "core-shell" structures is influenced by several factors, including the size of the initial primary domains and the viscosity. The growth mechanism of the secondary droplets in the late stage of coarsening ($r^3 > 6r_0^3$) obeys the power-law equation $r \propto t^n$, and the exponent n increases with decreasing viscosity coefficient.

The model developed and results obtained could shed light on utilizing spinodal decomposition in immiscible polymer systems to obtain unique nanostructures for advanced applications. The extension of the model into 3D is straightforward and corresponding work is underway.

ACKNOWLEDGMENTS

The work is supported by the National Natural Science Foundation of China (Grant No. 50425101) (X.J.L.), the Ministry of Education, P.R. China (Grant No. 707037) (X.J.L.), Xiamen City Department of Science & Technology (Grant No. 3502Z20093001) (C.P.W.), and the US National Science Foundation (Grant No. 0606417) (Y.W.).

[1] D. R. Paul and S. Newman, *Polymer Blends* (Academic, New York, 1978).
[2] I. Podariu and A. Chakrabarti, J. Chem. Phys. **126**, 154509 (2007).
[3] P. van de Witte, P. J. Dijkstra, J. W. A. van den Berg, and J. Feijen, J. Membrane Sci. **117**, 1 (1996).
[4] P. K. Chan and A. D. Rey, Macromolecules **30**, 2135 (1997).
[5] B. F. Barton, J. L. Reeve, and A. J. McHugh, J. Polym. Sci. Polym. Phys. **35**, 569 (1997).
[6] H. Tanaka, Phys. Rev. E **47**, 2946 (1993).
[7] K. D. Kwak, M. Okada, T. Chiba, and T. Nose, Macromolecules **26**, 4047 (1993).
[8] T. Sigehuzi and H. Tanaka, Phys. Rev. E **70**, 051504 (2004).
[9] T. Hashimoto, M. Hayashi, and H. Jinnai, J. Chem. Phys. **112**, 6886 (2000).
[10] M. Hayashi, H. Jinnai, and T. Hashimoto, J. Chem. Phys. **113**, 3414 (2000).
[11] J. Tao, M. Okada, T. Nose, and T. Chiba, Polymer **36**, 3909 (1995).
[12] N. Clarke, Phys. Rev. Lett. **89**, 215506 (2002).
[13] I. C. Henderson and N. Clarke, Macromolecules **37**, 1952 (2004).
[14] T. L. Tran, P. K. Chan, and D. Rousseau, Comput. Mater. Sci. **37**, 328 (2006).
[15] Y. Huang, R. Wang, Y. Sun, G. X. Li, G. L. Chen, and Q. Yang, Acta Mater. **56**, 1173 (2008).
[16] L. T. Yan, J. L. Li, F. B. Zhang, and X. M. Xie, J. Phys. Chem. **112**, 8499 (2008).
[17] P. G. de Genes, Rev. Mod. Phy. **64**, 645 (1992).
[18] Y. L. Yang, F. Qiu, H. D. Zhang, and J. W. Zhang, Prog. Nat. Sci. **8**, 513 (1998).
[19] E. Erturk, T. C. Corke, and C. Gokcol, Int. J. Numer. Methods Fluids **48**, 747 (2005).
[20] L. Ratke and S. Diefenbach, Mater. Sci. Eng. **R15**, 263 (1995).
[21] H. Tanaka, J. Chem. Phys. **105**, 10099 (1996).
[22] P. X. Ma, Adv. Drug Delivery Rev. **60**, 184 (2008).
[23] L. Li, R. G. Liu, S. Y. Zhang, and Z. F. Li, Liq. Cryst. **30**, 259 (2003).
[24] G. B. Wei and P. X. Ma, Biomaterials **25**, 4749 (2004).
[25] B. Zhou and A. C. Powell, J. Membr. Sci. **268**, 150 (2006).
[26] H. Tanaka, J. Chem. Phys. **105**, 10099 (1996).
[27] Y. R. Shang, D. Kazmer, M. Wei, J. Mead, and C. Barry, J. Chem. Phys. **128**, 224909 (2008).
[28] M. Fialkowski and R. Holyst, Macromol. Theory Simul. **17**, 263 (2008).
[29] E. L. Wolf, *Nanophysics and Nanotechnology* (Wiley-VCH, Weinheim, 2004).
[30] C. N. R. Rao, A. Muller, and A. K. Greetham, *The Chemistry of Nanomaterials* (Wiley-VCH, Weinheim, 2004).
[31] Y. Champion and H. J. Fecht, *Nano-Architectured and Nano-Structured Materials* (Wiley-VCH, Weinheim, 2004).
[32] S. Zhu, Y. Liu, M. H. Rafailovich, J. Sokolov, D. Gersappe, D. A. Winesett, and H. Ade, Nature (London) **400**, 49 (1999).
[33] P. J. Flory, *Principles of Polymer Chemistry* (Cornell University Press, New York, 1953).
[34] R. Koningsveld, W. H. Stockmayer, and E. Nies, *Polymer Phase Diagrams—A Textbook* (Oxford University Press, Oxford, UK, 2001).
[35] J. W. Cahn and J. E. Hilliard, J. Chem. Phys. **28**, 258 (1958).

[36] R. A. L. Jones and R. W. Richards, *Polymers at Surfaces and Interfaces* (Cambridge University Press, Cambridge, UK, 1999).
[37] G. Tegze, T. Pusztai, and L. Granasy, Mater. Sci. Eng. A **413-414**, 418 (2005).
[38] B. Nestler, A. A. Wheeler, L. Ratke, and C. Stocker, Physica D **141**, 133 (2000).
[39] D. Jacqmin, J. Comp. Phys. **155**, 96 (1999).
[40] A. G. Lamorgese and R. Mauri, Phys. Fluids **17**, 034107 (2005).
[41] I. M. Lifshitz and V. V. Slyozov, J. Phys. Chem. Solids **19**, 35 (1961).
[42] C. Shen, N. Zhou, and Y. Wang, Metall. Mater. Trans. A **39A**, 1630 (2008).
[43] L. Rayleigh, Proc. R. Soc. London **29**, 71 (1879).
[44] S. Tomotika, Proc. R. Soc. London, Ser. B **150**, 322 (1935).
[45] M. S. Miguel, M. Grant, and J. D. Gunton, Phys. Rev. A **31**, 1001 (1985).
[46] R. Almgren, A. Bertozzi, and M. P. Brenner, Phys. Fluids **8**, 1356 (1996).
[47] R. Almgren, Phys. Fluids **8**, 344 (1996).
[48] R. V. Da, and J. Barford, Nature (London) **217**, 1145 (1968).